Journal of The Electrochemical Society

The Electrochemical Society
Advancing solid state & electrochemical science & technology

OPEN ACCESS

Methods—Ampero-Coulometry: A New Technique for Understanding Lithium-Sulfur Electrochemistry

To cite this article: Umair Gulzar *et al* 2023 *J. Electrochem. Soc.* **170** 030503

Journal of The Electrochemical Society, 2023 **170** 030503

Methods—Ampero-Coulometry: A New Technique for Understanding Lithium-Sulfur Electrochemistry

Umair Gulzar,[1,*,z] Alex Lonergan,[1,*] Vladimir Egorov,[1] Yan Zhang,[1,*] Alex Grant,[1] Aoife Carroll,[1] and Colm O'Dwyer[1,2,3,*,z]

[1]*School of Chemistry, University College Cork, Cork, T12 YN60, Ireland*
[2]*Micro-Nano Systems Centre, Tyndall National Institute, Lee Maltings, Cork, T12 R5CP, Ireland*
[3]*Environmental Research Institute, University College Cork, Cork T23 XE10, Ireland*

Despite limited commercial success, lithium sulfur technology (LST) is still far from competing existing Li-ion technology. One of the main reasons hindering the success of LST is the complexity of lithium-sulfur chemistry during electrochemical charging and discharging. Dissolution of sulfur species in the electrolyte solution exacerbates the difficulties of this system. Therefore, a comprehensive understanding of sulfur species and their kinetics during charge/discharge process is paramount for a high-performance lithium-sulfur battery. We present a new technique we refer to as Ampero-Coulometry, which takes the chronoamperometric (galvanostatic) charge-discharge curves and mathematically transforms them to a series of curves that reveal the cation diffusional rate inside carbon-sulfur porous electrodes at different states of charge/capacity. This technique allowed us to track the overall Li^+ ion diffusional rate inside a Li-S cell over a complete state of discharge. As dissolution of sulfur species and their interplay inside a porous sulfur electrode has a significant role in limiting Li-S battery capacity, and method allows correlation between the known mechanism of polysulfide dissolution, the kinetics of a sulfur electrode, and its response.
 [DOI: 10.1149/1945-7111/acbca0]

Manuscript submitted December 1, 2022; revised manuscript received January 19, 2023. Published March 7, 2023.

Supplementary material for this article is available online

Lithium-Sulfur (Li-S) technology has long been sought after as an alternative to lithium-ion technology for a variety of niche applications. One of the main advantages is that some Li-S cells can reach practical energy densities of 500–600 Wh kg^{-1} using cheaper, lighter and environmentally benign sulfur electrodes.[1] However, Li-S technology is limited by its low power density and modest cycling performance.[2] Key problems that include electrode degradation, solubility of active material (sulfur) inside electrolyte and consequent shuttle effect need to be addressed before its commercialization. The last two decades have seen significant effort in solving these problems where a lot of focus was put on improving power density and cycle life, often by developing new conductive host materials for the sulfur cathode.[3,4]

To address the shuttle effect, various strategies have been developed for polysulfide (PS) confinement using micro porous and polysulfide adsorbent materials.[5] Modifying separators with various inorganic and polar materials also proved to be effective against the shuttle effect.[6,7] Recently, concepts from catalysis have also been applied to Li-S batteries to improve sulfur utilization and cycling stability.[8,9] Despite significant progress, dissolution of polysulfides, their kinetics and diffusion in the electrolyte during cell operation is not yet clear. As the capacity and rate capability of Li-S battery is strongly linked to the complex interplay of PSs, understanding their intrinsic kinetics at electrode/electrolyte interface is necessary to reveal the full potential of LSBs.

The evolution of these PSs in liquid phase has been tracked using UV–vis,[10,11] IR,[12] LC,[13–15] NMR,[14,16] and some electrochemical[17–20] and theoretical methods[21,22] while their progressive deposition on electrode surfaces has been monitored using XRD and TEM measurements.[16,23–25] One of the most referenced studies is based on ex situ liquid chromatography coupled with UV–vis and electron spin resonance spectroscopy.[13] There, the authors proposed that $S_6^{-2}/S_3^{\bullet-}$ species of PSs are formed in first discharge plateau which subsequently reduced to S_4^{-2} during the transition region between 1st and 2nd plateau. During the second voltage plateau the S_4^{-2} species are subsequently reduced to $S_3^{\bullet-}$, S_2^{-2}, and S_1^{-2} forms, where S_1^{-2} corresponds to the deposition of Li_2S. Although the study provides an insight to the mechanism of PSs, these ex situ results do not necessarily represent real-time Li-S chemistry where all reactions are happening simultaneously in a fixed electrolyte system. To solve this problem, operando studies have been employed to track the formation and dissolution of PSs species inside working Li-S batteries.[24,26,27] In one study,[27] X-ray absorption spectroscopy was used to detect not only the amorphous and crystalline redox products (S_8 and Li_2S) but also the dissolved PSs. After monitoring PSs evolution during the charging process, the authors concluded that PSs species remains at relatively constant composition and concentrations. Unfortunately, their technique was unable to differentiate different PSs signals consequently limiting its use as tool for identifying PSs species inside electrolyte solution.

On the other hand, UV–vis spectroscopy stands out as a very practical technique to differentiate long and small chain chromophoric PSs inside electrolyte solution. Some of the earlier studies suggested that S_8^{-2} and $S_3^{\bullet-}$ radical ions are predominant in high donor number solvent[28–31] (i.e. DMSO and DMF) while S_4^{-2} show higher concentrations in low donor number solvents[32] including DOL: DME, the most commonly used electrolyte solvent in Li-S battery. Later Patel et al.[11] used UV–vis spectroscopy on a pouch cell and confirmed the presence of S_8^{-2} and S_6^{-2} species during 1st plateau, S_4^{-2} and $S_3^{\bullet-}$ species during 2nd plateau and lithium sulfide at the end of discharge curve. However, in a very recent study, Gasteiger's group[9] not only confirmed the presence of S_4^{-2} species in the first plateau but also identified a the trisulfide radical species $S_3^{\bullet-}$, which appears during transition stage between the 1st and 2nd plateaus. They showed that elemental S_8 is converted to S_4^{-2} during the 1st discharge plateau, where contrary to Patel's study, other polysulfides (i.e. S_8^{-2} and S_6^{-2}) are barely detected. These S_4^{-2} species get reduced to a meta-stable PS species $S_3^{\bullet-}$ in the transition stage of 1st and 2nd plateau and dominates the second discharge plateau. So far, UV–Vis spectroscopy has been the most successful technique to understand the formation and consumption of PSs inside electrolyte. However, these operando techniques detect only those PSs that can easily diffuse within the electrolyte during the experiment. Consequently, PSs with faster kinetics and lower diffusion are difficult to detect using these techniques. For example, Qi et al.[9] in their study suggested that it is quite possible that S_8^{-2}

*Electrochemical Society Member.
[z]E-mail: umair.gulzar@ucc.ie; c.odwyer@ucc.ie

species did convert to S_6^{-2} species during the 1st plateau, however, due to lower diffusion and fast kinetics, quickly converted into S_4^{-2} species, hence not detectable in electrolyte.

Electrochemical techniques such as cyclic voltammetry and chronoamperometry are powerful as they provide information on PSs interplay at electrode/electrolyte interface. In one such case, Patrick et al.[21] provided a quantitative insight into the reaction mechanism of PSs using cyclic voltammetry at different depths of discharge. They suggested that the performance of a Li-S battery is strongly linked to chemical disproportionation and the equilibrium between multiple PSs species. Ma et al.[33] used an H-type electrolytic cell to quantitatively measure the intrinsic kinetics of various PSs conversions. They used steady state polarization curves to obtain redox potentials, exchange current densities, reaction orders and activation energy for PSs conversion. These results, in particular Tafel slopes and exchange current density, were used to predict the mechanism of PSs dissolution and their influence on a typical charge discharge profile of Li-S battery.

Chronopotentiometry (CP), chronoamperometry (CA) and chronocoulometry (CC) belong to a family of electrochemical techniques that involve an application of "step" potential or current. In case of CP, a "step" current is applied while change in potential is measured against time. Also known in battery community as galvanostatic or constant current method, this technique is widely applied to obtain a charge/discharge profile of a battery and also used to understand electrode behavior. On the other hand, CA and CC methods apply a "step" voltage to observe current and charge, respectively, against passing time. Although less commonly used, both methods are the fastest way of charging or discharging a battery. For experiments where $t \rightarrow \infty$, the capacities are equal to nominal capacities, however, for realistic experimental durations (i.e. $t \ll \infty$), the capacities obtained are somewhat less than the nominal capacity. This is due to the fact that reactions with faster rates have sufficient time to take place in some systems. In this sense, a current transient in CA contains information on the rate capability of a cell[34,35] which can be used to understand electrode kinetics. Recently, CA and CC have been utilized in addressing specific issues related to interfacial kinetics[36–38] and diffusion phenomena.[39,40] In particular, Heubner et al.[34] used a simple CA method to determine that rate capability of porous electrodes in LIB. They showed that the CA response can be mathematically transformed into C-rates which are comparable to the C-rates obtained using conventional CP method. Later, Tian et al.[41] modified Heubner's work to predict C-rate over a longer range using a more realistic approach. Instead of using theoretical capacities, they used true capacities of a working LIB enabling them to predict C-rate more accurately over a long range.

In our effort to understand the kinetics of PSs inside a working Li-S cell, we used chronoamperometric experiments to develop a new technique named Ampero-Coulometry (AC). The technique uses experimental data from CA and mathematically transforms them to reveal diffusional rate inside carbon-sulfur porous electrodes over a complete state of discharge. As dissolution of PSs and their interplay inside a porous sulfur electrode has a significant role in limiting Li-S battery capacity, we were able to relate the known mechanism of PSs dissolution with the kinetics of sulfur electrodes and its performance. The method also provides this information in a much shorter timeframe compared to longer term cycling measurements, and is generally applicable to any battery, supercapacitor or electrochemical system where galvanostatic and/or potentiostatic measurements are made.

Experimental

Materials preparation.—Carbon-Sulfur composites were prepared by mixing elemental sulfur (99.998% trace metal basis, Sigma Aldrich) with Super-P conductive carbon black (TIMCAL, MTI Corporation) in weight ratios of 7:3. After grinding, the mixture was heated at 155 °C in an inert atmosphere in order to melt diffuse sulfur inside the carbon matrix.

Materials characterization.—The morphology of sulfur electrodes was evaluated using scanning electron microscopy (SEM) images obtained from a FEI Quanta 650 SEM operated at spot size 3 and 15 kV beam voltage. Energy dispersive X-ray analysis was also performed to track the distribution of sulfur onto the surface of electrodes. Raman scattering analysis of carbon black and C/S composite was carried out using a Renishaw inVia Raman spectrometer in conjunction with a 30-mW Ar^+ laser at an excitation wavelength of 514 nm. The laser was focused using a 40 × objective lens and signals were collected using a RenCam charge-coupled device (CCD) camera. The crystal structure of the sulfur was confirmed by X-ray diffraction (XRD) using a Philips X'pert Pro MPD equipped with a Panalytical Empyrean Cu X-ray tube and a Philips X'celerator detector. Thermogravimetric analysis was carried out using a Perkin Elmer TGA 4000 instrument. Samples of C/S composite were heated at a ramp rate of 5 °C min^{-1} from room temperature to 600 °C under an inert atmosphere.

Li-S cell fabrication and electrochemical characterization.—Cathode slurries were prepared by grinding C/S composites, Super-P conductive carbon black and multiwalled carbon nanotubes (MWCNTs) in a water suspension of carboxymethyl cellulose/styrene butadiene rubber (CMC-SBR) binder (MTI Corporation). Ethanol was used to adjust the viscosity of as-prepared slurry. The final slurry consists of 80% C/S composite, 11% Super-P conductive carbon, 8% CMC-SBR binder and 1% MWCNTs. Electrodes were prepared by coating slurries on aluminum (Al) sheets (20 μm thickness) using a doctor blade and cut into discs (area = 0.78 cm^2). Electrodes were not pressed in order to achieve maximum areal porosity and PSs dissolution. The average thickness of each electrode (incl. Al current collector) was 130 μm while the average areal mass loading was 2.0 $mg_{(s)}$ cm^{-2}. Geometrical porosity (p_g) was calculated using Eq. 1,

$$p_g = \frac{V_g - V_d}{V_g} \quad [1]$$

where V_g and V_d are the geometrical and dense volume of the C/S electrode. The geometrical volume was calculated as $V_g = \pi r^2 t$ where t is the electrode thickness. The dense volume $V_d$was calculated using the density and relative mass of each electrode material.

Electrochemical testing was carried out using 0.78 cm^2 circular Lithium disks (Sigma Aldrich) as a reference electrode and as-prepared C/S composite based cathode. These electrodes were separated by glass fiber separator (Whatman GF/D) soaked with 60 μl electrolyte solution which consist of 0.4 M LiTFSi, 0.6 M $LiNO_3$ and DOL: DME (1:1). Electrodes were assembled in a PAT test cell (EL-CELL), connected to PAT-stand-4 docking station (EL-CELL) and placed inside temperature-controlled environment to maintain a constant temperature of 25°C. Chronoamperometry (CA) and galvanostatic chronopotentiometry (CP) experiments were performed using VMP3 multichannel potentiostat (Biologic) controlled by EC Lab software. Initially, five CP cycles were performed on each cell at 0.1 C followed by a CA experiment. For step-chronoamperometry, three voltage steps (2.20 V, 1.90 V, and 1.80 V) were chosen based on the discharge profile obtained from chronopotentiometry. The electrochemical methods leading to the ampero-coulometric curve outlined later are depicted below in Fig. 1 schematically. Starting with a standard galvanostatic discharge curve at constant current in Fig. 1a, the cell then undergoes a chronoamperometric measurement depicted in Fig. 1b at constant potential. This potential is equivalent to the cutoff potential V_1 of the discharge curve from Fig. 1a and is applied for a time equivalent to the time t_1 taken to reach a value of current that is identical to the applied current I_1 in galvanostatic measurements. Once the current is integrated (Fig. 1c) to a charge, the charge can be converted to AC curve as we discuss further on.

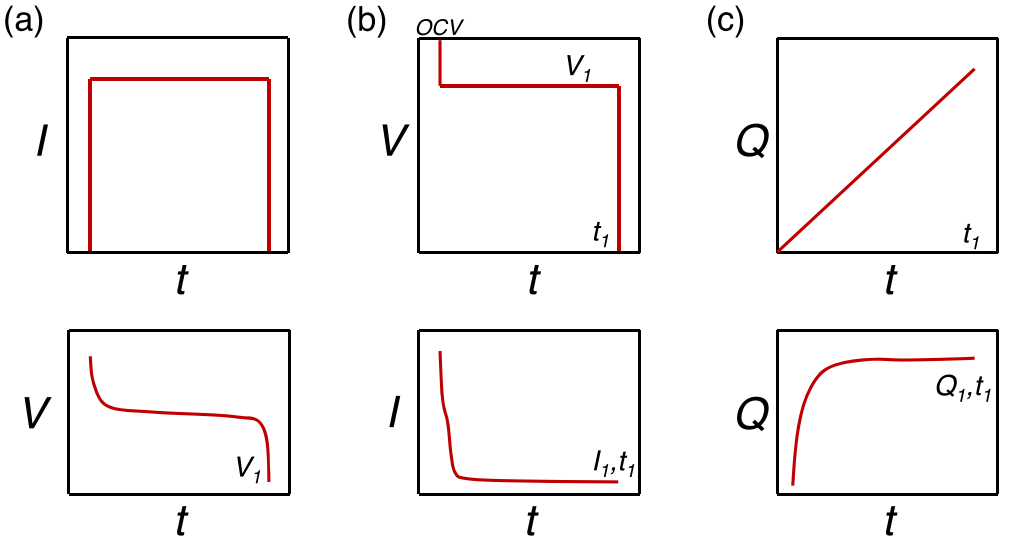

Figure 1. Schematic representation of the various electrochemical measurements of the Li-S battery including (a) galvanostatic measurements (chronopotentiometry) at an applied current I_1, (b) chronoamperometry acquired from OCV to a potential equivalent to the cutoff lower potential V_1 from (a). The potential is applied for time t_1 equal to the time taken to reach a value of current I_1 identical to that of the applied current in (a), and (c), integration of the measured current up to time t_1.

Results and Discussion

Porous carbon-sulfur cathodes.—Figure 2 details the nature of the porous C/S cathode used in this ampero-coulometric analysis. Once cast, the C/S composite electrode material was first analyzed using Raman spectroscopy. Figure 2a shows two prominent D and G peaks at 1357 and 1597 cm^{-1}, respectively known from disordered and defective sp^2 carbon and the second peak at 1597 cm^{-1} is related to the vibrational modes of graphitic carbons.[42] The I_D/I_G ratio was close to unity which can be explained by the defective nature of conductive carbon matrix.[19] Moreover, a broad peak between 250 and 450 cm^{-1} can be linked to sulfur encapsulated inside carbon matrix[43] while the peak centered at 800 cm^{-1} can be attributed to glass substrate.[44,45] The data also showed a peak at 2276 cm^{-1} from functional group impurities (C–H, C–O, C–S). XRD analysis also confirmed the presence of elemental sulfur (Fig. 2b) where all reflections (those indexed and marked and remaining peaks) match with JCPDS 08–0247. The C−S composite showed typical peaks associated with highly crystalline sulfur on a broad carbon peak centered at 25°, with the full XRD spectrum show in the Supplementary Materials, Fig. S1.

The sulfur content was uniformly distributed over the morphology of the overall composite materials as seen in SEM and EDX data in Figs. 2c,2d and at higher magnification in Fig. S2, Supplementary Material. These findings were confirmed using high resolution core-level photoemission spectrum from S 2p in Fig. 2e suggesting that some of the sulfur is chemically linked to the carbon matrix.[46] These peaks can be assigned to aromatic sulfur (162.3 eV), S−C group (164.4 eV), S−O−C group (165.5 eV) and

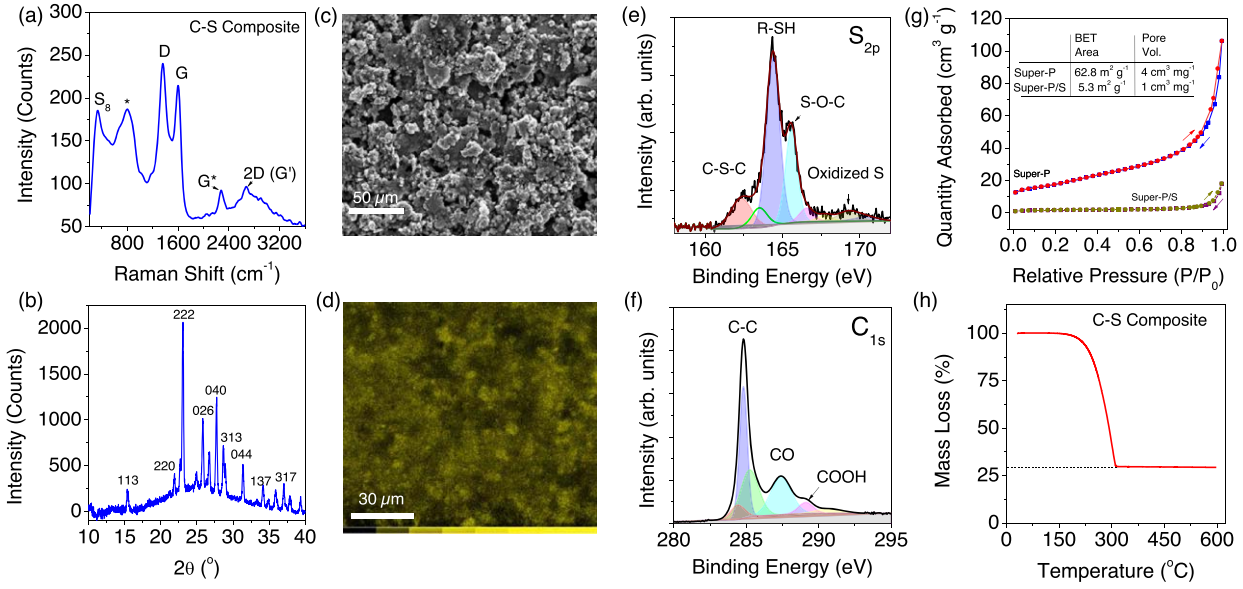

Figure 2. (a) Raman scattering spectrum and (b) XRD diffraction pattern of the C-S composite material indexed to JCPDS 08–0247. (c) SEM and (d) EDX map of the C-S composite, the light yellow-green color in the EDX map represents elemental sulfur. (e,f) X-ray photoelectron spectra from S 2p and C 1 s core levels. (g) N_2 adsorption/desorption isotherms for the C/S and the non-sulfur containing super-P carbon, with BET calculated surface areas and pore volumes. (h) Thermogravimetric analysis of the C/S composite.

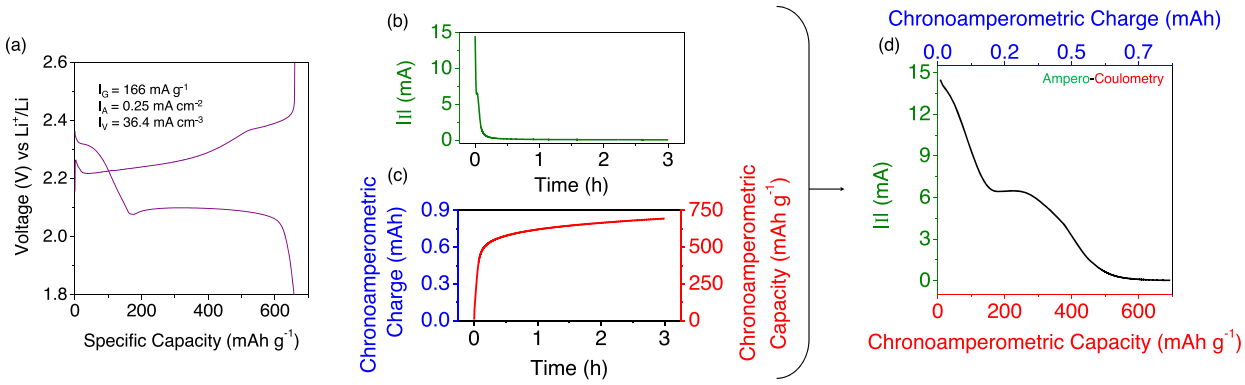

Figure 3. (a) Charge-discharge curve for the Li-S cell at a specific current of 166 mA g^{-1}, corresponding to 0.25 mA cm^{-2}. (b) Current vs time plots obtained after chronoamperometric experiment performed on the Li–S cell at a constant potential of 1.8 V (cutoff from the galvanostatic discharge). (c) Chronocoulometric plot obtained by integrating the current in (b) over time. (d) Ampero-coulometric plot obtained by plotting current against the state of charge (gravimetric capacity). (e) Schematic summary of the applied currents and potentials for each measurement type shown in (a)-(d).

other oxidized sulfur species (169.2 eV).[47] In the C 1 s core-level in Fig. 2f, we note three prominent peaks at 284.8, 287.4 and 289.6 eV can be attributed to C−C, C−O and C = O groups, respectively.

N_2 physisorption analysis was performed to determine the surface area and pore size distribution of the as-prepared C/S composite. Figure 2g shows N_2 adsorption/desorption isotherm obtained for conductive super-P and C/S composite. Pristine conductive super-P carbon showed a type II isotherm indicating macro pore sizes >50 nm.[48] Total surface area and pore volumes of pristine conductive Super-P carbon were found to be 62.8 m^2 g^{-1} and 0.004 cm^3 g^{-1}, respectively while the C/S composite showed a significantly lower value (5.3 m^2 g^{-1}) due to sulfur encapsulation of majority of the pore volume. Thermogravimetric analysis (TGA) was used to determine the sulfur content in C/S composites and in Fig. 2h illustrates a sharp decrease in weight when temperature increases from 115 to 300 °C corresponding to the removal of sulfur. TGA results also confirmed that sulfur accounts for ∼70% of the total weight in C/S composites. Geometrical porosity of C/S composite electrodes was calculated using Eq. 1, and lies in the range of 75%–80%.

The ampero-coulometry method.—Figure 3a shows a typical chronopotentiometric V(t) response of the C/S Li-S cell cathode commonly referred to as a galvanostatic charge-discharge, and for reference we also show the first five charge/discharge cycles of a similar cell in Supplementary Materials, Fig. S3. The response (Fig. 3a, the 5th cycle) is characteristic of a Li-S cell with a Li metal anode. In tandem, we also ran a chronoamperometric (CA) I(t) response curve shown in Fig. 3b, where a potential of 1.8 V (corresponding to the lower cutoff of the galvanostatic discharge in Fig. 3a) is applied. This method has been used recently to very quickly characterize the rate behavior (capacity vs. rate) of an batteries across a wide range of C-rates in a much shorter time compared to standard rate-dependent galvanostatic cycle life tests.[34,35,49–51] This CA curve can then be transformed into a chronocoulometric curve by simply integrating the current over the course of experiment, as we show in Fig. 3c. By combining the two curves in Fig. 3b and 3c (i.e. plotting I vs Q) results in a curve in Fig. 3d, which we call an ampero-coulometric (AC) curve. As will be shown, this curve is sensitive to, and reveals, the processes involved in a Li–S battery. One of the main advantages of this method is that it allows the capacities obtained from chronopotentiometry (CP) or galvanostatic discharge to be compared or superimposed with chronoamperometric (CA) discharge profile, when the CA current is limited to the applied current or C-rate used in the CP method. It is important to mention that generally there is no cutoff current in a CA measurement. To compare it to the discharge profile obtained from CP method at 0.1 C (0.170 mA), we limited the current according to that value. If we were to discharge our Li-S cell at 0.01 C (0.0170 mA) in a galvanostatic CP measurement, we would stop our experiment at 0.0170 mA in CA method.

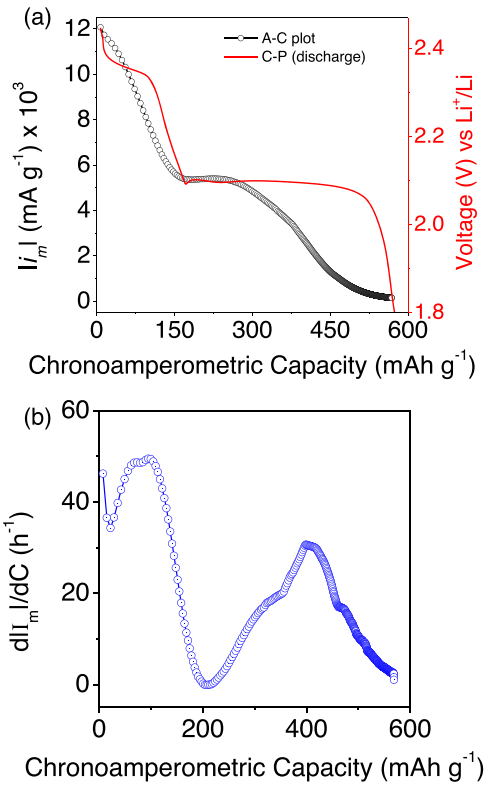

Figure 4. (a) Ampero-coulometric plots obtained from chronoamperometric experiment on the Li-S cell. (b) Differential ampero-coulometric curve obtained from the slopes of ampero-coulometric plot in (a).

In our case, we discharge a Li–S cell using a CP method by drawing a constant current of 0.170 mA (0.1 C). After charging, the cell was subjected to chronoamperometry where the cutoff voltage was set to 1.8 V. The experiment was stopped when the current reaches the value of 0.170 mA which is equal to the constant current applied in CP method. The chronoamperometric capacities obtained from CA method were plotted against current and compared with the gravimetric capacity obtained from CP method. By comparing to other reports involving potential step methods transformed to rate behavior,[41,49] we found that capacity obtained from CP method (573

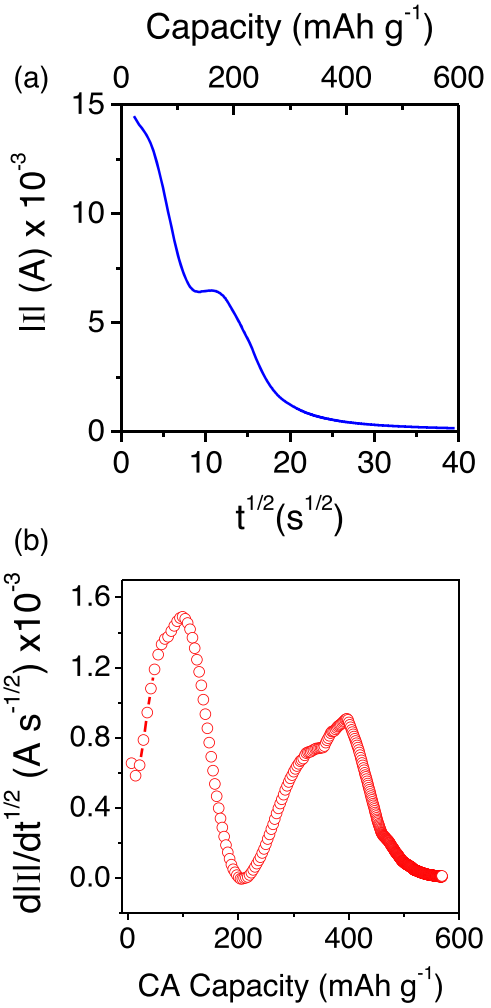

Figure 5. Cottrell plot (i vs $t^{1/2}$) obtained from chronoamperometric (CA) experiment data. (b) Slope of the Cottrell plot as a function of capacity obtained from chronoamperometric measurements.

mAh g^{-1}) was almost equal to the capacity obtained from CA method (568 mAh g^{-1}) if the experiment is stopped at a limiting current of 0.170 mA (i.e. the constant current used in CP method). As CA method is the fastest way of charging/discharging a battery, time required to discharge our Li–S cell using CA method (0.43 h) was 9.5 × less than the CP method (4.1 h). Such fast electrode/cell assessment times are possible with careful use of CA curves and can always be compared to standard CP (galvanostatic) curves for comparison/checking.

Figure 4a shows a typical discharge curve of Li–S cell obtained from CP method which is superimposed with an ampere-coulometeric curve obtained for the same Li–S cell. Although the two curves show similar capacities, the AC curve displays a reducing slope that finishes when the capacity reaches a value of 170 mAh g^{-1}. A relatively flat region was observed from 170–280 mAh g^{-1} followed by another decreasing slope which flattens as it reaches the maximum capacity of 567 mAh g^{-1}. On the other hand, CP curve showed an upper and lower plateau at 2.43 and 2.1 V respectively. It is important to mention that both these plateaus are not flat and detailed inspection of CP curve and its relation to ampere-coulometric (AC) curve will be discussed further on.

By differentiating the ampero-coulometric (AC) curve and plotting its slope $\frac{dI_m}{dC}$ against capacity, we were able to produce a differential amperometric capacity plot showing two prominent peaks in the region 0–170 mAh g^{-1} and 170–570 mAh g^{-1} (Fig. 4b). Interestingly these peaks lie in the same region of the two upper and lower plateaus usually obtained using CP method. Although the quantity $\frac{dI_m}{dC}$ seems dimensionally similar to C-rate (i.e. h^{-1}), the C-rate has a specific definition strictly related to CP charge-discharge curves. For example, complete discharge at 1 C rate in 1 h requires a constant discharge current (i). As the current is constantly decreasing in CA method, the strict definition of C-rate used in CP method is not applicable. Although Tian et al.[41] and Heubner's et al.[34] have used the concept of C-rate in their CA method, due to different mathematical transformation used in our case, we define the quantity $\frac{dI_m}{dC}$ as a diffusional rate instead of the C-rate. In this context the diffusional rate represents the rate of change of current during the state-of-charge in the Li–S cell and reveals useful information about the kinetics of Li–S electrochemistry. Plotting $\frac{dI_m}{dC}$ or diffusional rate against time resulted in a differential ampero-coulometric (AC) plot which can be compared with CP discharge curve allowing us to correlate the interplay of PS species and their effect on diffusional rates and the kinetics of Li−S cell.

Before making these linkages, we also sought to understand the connection between the differential ampero-coulometric representation and diffusional kinetics within electrodes. The data is reminiscent also of the Cottrell relation for a diffusion limited system and so we produced a Cottrell plot (i vs $t^{1/2}$) (Fig. 5a) from the same CA data in Fig. 2. Interestingly, the overall shape of the Cottrell curve in Fig. 5a is very similar to the AC curve (Fig. 3a) where the decreasing slope is followed by plateau and a second decreasing slope. This current-time response observed in Fig. 5a can be represented by the Cottrell equation (Eq. 2)

$$i = \left(\sqrt{\frac{D}{\pi}} FAC_0\right) t^{-1/2} \qquad [2]$$

where D is the diffusion coefficient in $cm^2\ s^{-1}$, F is the Faraday constant (96,485 C mol^{-1}), A is the area of sulfur electrode in cm^2, C_0 is the concentration of Li^+ ions inside electrolyte solution (presumably crowded with PSs) in mol cm^{-3}, and t is the time in sec.

Using the same Eq. 2 we were able to mathematically correlate the similar shapes observed in both Cottrell and ampero-coulometric (AC) plots.

Squaring Eq. 2 on both sides gives

$$i^2 = \frac{\left(\frac{D}{\pi} F^2A^2C_0^2\right)}{t} or\ i = \frac{\left(\frac{D}{\pi} F^2A^2C_0^2\right)}{it} \qquad [3]$$

where $Q = it$ in coulombs. In order to convert Q into specific capacity (C_s) and i into specific current i_m we scale with the capacity (in this example, $C = 0.2778$ mAh) and the mass of active material which gives

$$i_m = \frac{1}{C_s}\left(\frac{DF^2A^2C_0^2}{C\pi m_s^2}\right) \qquad [4]$$

where i_m is the current density (mA g^{-1}), C is the capacity (mAh g^{-1}) and m_s is the mass of active material. As the form of Eqs. 2 and 3 are similar, associated plots yield similar shapes (Figs. 4a and 5a). The derivative of Eq. 4, i.e. $\frac{dI_m}{dC}$ gives

$$\frac{dI_m}{dC_s} = -\frac{1}{C_s^2}\left(\frac{DF^2A^2C_0^2}{C\ \pi\ m_s^2}\right) \qquad [5]$$

which links the differential ampero-coulometric rate, or diffusional rate $\frac{dI_m}{dC_s}$, to the diffusion constant D of Li^+ ions. Figure 5b shows

the slope of the Cottrell relation from Fig. 5a as a function of the capacity from the CA data and we can see the correlation or similarity of the plot to the AC method being proposed here suggesting that the diffusion-limited behavior of the Li^+ ions is a suitable relative "tracer" for the diffusion-limited processes and their rate variation in the Li-S system, at least to assess the AC technique and trends in potential step measurements via the Cottrell relation to typical galvanostatic data. As the dissolution of PS inside the electrolyte affects the diffusion of Li^+ ions, it should also affect diffusional rate over the course of discharge.

In Fig. 6a we present a differential ampero-coulometric plot obtained from CA data and superimposed with the discharge profile obtained from CP method at 0.1 C (0.170 mA g^{-1}). Depending on the change in diffusional rate, we divided this plot into four regions. Discharging a Li−S cell involves Li^+ ion diffusion towards the sulfur electrode and the associated rate of diffusion should decrease as the cell approaches its full state-of-discharge. However, we believe that dissolution of PSs and their diffusion towards the opposite Li electrode will affect the Li^+ diffusion rate. Therefore, as the concentration of PSs species inside electrolyte/electrode interface changes, the rate of cation diffusion should also modify accordingly. These changes are clearly visible in Fig. 6a where the diffusional rates are elevated and then decrease in "waves" as the battery moves towards complete discharge. At first, an increase of diffusional rate was observed until the capacity reaches the value of 100 mAh g^{-1} (Region I). We believe that the increase in diffusional rate is the result of unused PS species that did not convert to sulfur during the previous charging process. During the voltage window of Region I, (to 2.2 V), the reaction follows $S_8^{-2} + 2Li^+ + 2e^- \overset{R_1}{\Leftrightarrow} Li_2S_6$ at a rate R_1. Readers can refer to Fig. S4, Supplementary Material, for an expanded view of each of Regions I—IV.

During the subsequent CA experiment, these PSs are the first to get reduced thereby clearing up excess PSs species at the porous electrode surface. As the PS concentration decreases inside the pores, diffusional rate of Li^+ ion towards the sulfur electrode should increase as shown in Fig. 6a, Region I. Once the accessible PSs have been utilized, the sulfur electrode starts producing higher order PSs (S_8 to S_6) to be dissolved inside electrolyte. A higher PSs concentration inside the porous electrode will likely hinder the diffusional rate for Li^+ ions, hence, decreasing the diffusional rate (Fig. 6a, Region II). Here, the process follows $S_8^{-2} + 4Li^+ + 4e^- \overset{R_2}{\Leftrightarrow} 2Li_2S_4$ at a rate $R_2 < R_1$. The cation diffusional rate in this region (see Supplementary Material, Fig. S5) also reaches its lowest value as the capacity approaches 200 mAh g^{-1}, which is also the end of 1st plateau region and the start of 2nd plateau region (Fig. 6a, Region III). As the concentration of S_6 species reduces, R_1 can again increase stabilizing the total cell rate which contains contributions from R_1 and R_2.

Recently, Kang et al.[52] have suggested that end of first plateau region is the result of PSs concentration reaching a maximum inside the porous electrode. These results are consistent with our differential ampero-coulometric plot where diffusional rates associated with the overall reaction reach their minimum value at the end of first discharge plateau. Comparison to parallel measurement from potential step data in the framework of the Cottrell equation for Li^+ cation diffusion (Fig. S5) also show this trend. Afterwards, the diffusional rates increase in Fig. 6, Region III until the capacity reaches 400 mAh g^{-1}. In this region, PSs of higher order dissociate to smaller PSs species via $S_8^{-2} + 16Li^+ + 16e^- \overset{R_2}{\Leftrightarrow} 8Li_2S$ as reported elsewhere.[9,11]

Due to their smaller size and higher solubility in the electrolyte, these low order PSs (S_4 and S_2) move out of porous regions into the separator, hence reducing the concentration of PSs in the cathode and increasing the diffusional rate local to (unblocking) the cathode surfaces. This kinetic change can be observed in the green region of CP discharge profile (and for comparison also in Fig. 5b) where we see the voltage rise until the capacity reaches the value of ∼400 mAh g^{-1}. Finally, the remaining lower order PSs convert into lithium sulfide and deposit onto the porous electrode surface. The diffusion inside the solid lithium sulfide is translated in the Region IV of our differential ampero-coulometric plot (Fig. 6a) where diffusional rates reach their second lowest values due to the blocking nature of lithium sulfide particles. To verify that our differential ampere-coulometric plots are reproducible and correspond to the assigned region of a typical CP discharge curve, we repeated CA measurements on the same cell at different voltage steps of 2.2, 1.9 and 1.8 V (Figs. 6b, 6c). The step voltages were selected based on the known PSs dissolution mechanism identified above where higher PSs are produced in the rage of 2.4–2.2 V, smaller order PSs are produced from 2.1–1.9 V while deposition of Li_2S happens at the end of discharge (1.9–1.8 V). The rationale behind this experiment was to confirm whether the shape of CA curve obtained with a 1.8 V cutoff corresponds to assigned polysulfide processes. We hypothesized that if the shape of CA curves obtained at these small potential steps (2.2, 1.9, and 1.8 V) correspond with the sections of CA curve obtained with a 1.8 V cutoff, then the polysulfide dissolution processes, which are voltage dependent, must be linked to that particular section of the curve, hence the dissolution process.

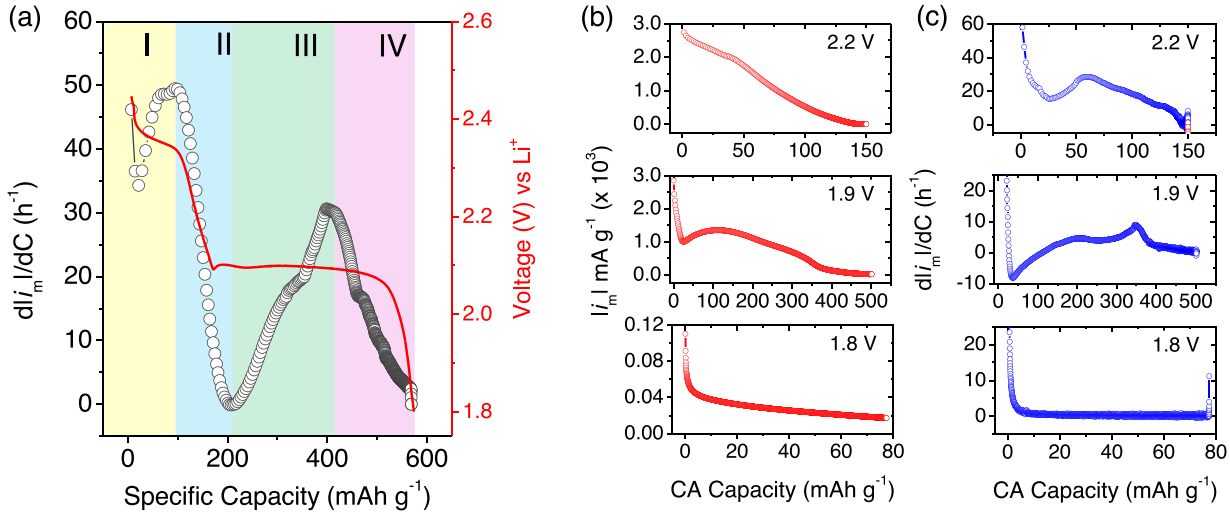

Figure 6. (a) Differential ampero-coulometric plot (black) and chronopotentiometric discharge profile (red) of Li-S cell distributed in four regions (I-IV) showing kinetic processes related to S_x^{-2} production, $x \geqslant 6$ (I), S_x^{-2} buildup, $x \geqslant 6$ (II), S_x^{-2} production, $x \geqslant 2$ (III), and Li_2S formation (IV). (b) Amperocoulometric and (c) differential ampero-coulometric plots obtained at potentials steps of 2.2 V, 1.9 V, and 1.8 V.

Figures 6b and 6c show AC plot along with differential AC curves $\left(\frac{dI_m}{dC_s}\right)$ obtained at a step voltage of 2.2, 1.9 and 1.8 V. It is evident that the profile of the curves in Figs. 6b, 6c match well with the individual sections of the curve in Figs. 4a,4b where first current decreases linearly (similar to Fig. 6b, 2.2V) followed by a hump (consistent with Fig. 6b, 1.9V) and further decrease until it reaches a plateau (corresponding to Fig. 6b, 1.8 V). Consequently, it proves our hypothesis that the diffusional processes we assigned to the individual sections of the Figs. 4a, 4b correspond to the processes that occur during these voltage ranges (i.e. 2.2, 1.9, 1.8 V). Moreover, the capacities obtained in these potential step plots (150 mAh g^{-1} at 2.2 V, 500 mAh g^{-1} at 1.9 V and 80 mAh g^{-1} at 1.8 V) are similar to the capacity obtained during relevant sections of the AC curves in Figs. 4a, 4b. However, due to smaller potential step from open circuit (2.2 V), the current and capacity obtained in these plots (Figs. 6b, 6c) are expectedly a little lower compared to the ampero-coulometric plot shown earlier in Figs. 4a, 4b. Nevertheless, these plots confirm that the change in diffusional rate in regions I and II are related to upper plateau of the CP discharge profile.

While the Cottrell plot analysis showed a remarkable similarity to the ampero-coulometric curve in shape, its diffusion limited response is often assumed to be representative of cation diffusion, whereas the Li-S system involved PSs that are also mobile. For comparison we also estimated the diffusion constants from the Cottrell relation and these can be found in Fig. S5, Supplementary Material. Although the processes in the Li-S system involve PSs, the Li^+ cations are involved in all reactions for PS formation and tracking Li^+ diffusion constant is an indicator for cation diffusion up to the point where PSs in various orders are formed. For comparison, D for PSs (down to Li_2S_4) are reported in the range $\sim$1.5–2.0 $\times$ 10^{-11} cm^2 s^{-1} and our estimates of D_{Li} range from 1–13 $\times$ 10^{-10} cm^2 s^{-1} over the entire discharge, closely following the response from AC data. All these observations suggest that our ampero-coulometric data is a simple and useful way of correlating kinetics of Li−S system with the state of discharge involving both the Li^+ diffusion and the reaction rate associated with PS formation, dissolution, diffusion and deposition. As shown, once Li_2S deposition occurs, the diffusion rate (and representative Li^+ diffusion constant) are severely retarded and total capacity becomes limited.

Conclusions

We have developed a simple ampere-coulometric technique to understand the kinetics of a typical Li−S cell. Our technique uses a simple mathematical transformation of chronoamperometric data (I vs t) and reveals useful information on the diffusion of Li^+ inside a Li−S cell. Moreover, it allows a comparison and simultaneous observation of the kinetic and thermodynamic changes inside a Li−S cell. Applying this method during the discharging of Li−S cell revealed more information on PS dissolution and their shuttle effect. The rate-related technique is useful in identifying the ranges of voltage where the shuttle effect takes place and may prove useful for Li-S cells when parameters such as sulfur or carbon loading are modified, when porosity is varied or with different electrolyte concentrations, type etc are introduced. The approach in principle is also amenable to other electrochemical systems and we hope others might find it to be a useful tool for interpreting or comparing the response of materials or cells with more sensitivity compared to differential capacity data or related approaches, while doing so over shorter experimental times.

Acknowledgments

Supporting from the Irish Research Council under an Advanced Laureate Award (IRCLA/19/118) and Government of Ireland Postdoctoral Fellowship (GOIPD/2021/438) are gratefully acknowledged. Support is also acknowledged from the European Union's Horizon 2020 research and innovation program under grant agreement No 825114. This work is partly supported by Enterprise Ireland Commercialisation Fund as part of the European Regional Development Fund under contract no. CF-2018–0839-P.

ORCID

Colm O'Dwyer https://orcid.org/0000-0001-7429-015X

References

1. X. Yang, X. Li, K. Adair, H. Zhang, and X. Sun, *Electrochemical Energy Reviews*, **1**, 239 (2018).
2. S. Dörfler, H. Althues, P. Härtel, T. Abendroth, B. Schumm, and S. Kaskel, *Joule*, **4**, 539 (2020).
3. F. Li, Q. Liu, J. Hu, Y. Feng, P. He, and J. Ma, *Nanoscale*, **11**, 15418 (2019).
4. T. Li, X. Bai, U. Gulzar, Y. J. Bai, C. Capiglia, W. Deng, X. Zhou, Z. Liu, Z. Feng, and R. Proietti Zaccaria, *Adv. Funct. Mater.*, **29**, 1901730 (2019).
5. W. Ren, W. Ma, S. Zhang, and B. Tang, *Energy Storage Mater.*, **23**, 707 (2019).
6. N. Deng, Y. Wang, J. Yan, J. Ju, Z. Li, L. Fan, H. Zhao, W. Kang, and B. Cheng, *J. Power Sources*, **362**, 243 (2017).
7. X. Yu, J. Joseph, and A. Manthiram, *J. Mater. Chem. A*, **3**, 15683 (2015).
8. H. Wu, H. Jiang, Y. Yang, C. Hou, H. Zhao, R. Xiao, and H. Wang, *J. Mater. Chem. A*, **8**, 14498 (2020).
9. Z. Ye, Y. Jiang, L. Li, F. Wu, and R. Chen, *Adv. Mater.*, **32**, e2002168 (2020).
10. Q. He, A. T. S. Freiberg, M. U. M. Patel, S. Qian, and H. A. Gasteiger, *J. Electrochem. Soc.*, **167**, 080508 (2020).
11. M. U. Patel, R. Demir-Cakan, M. Morcrette, J. M. Tarascon, M. Gaberscek, and R. Dominko, *ChemSusChem*, **6**, 1177 (2013).
12. N. Saqib, G. M. Ohlhausen, and J. M. Porter, *J. Power Sources*, **364**, 266 (2017).
13. C. Barchasz, F. Molton, C. Duboc, J. C. Lepretre, S. Patoux, and F. Alloin, *Anal. Chem.*, **84**, 3973 (2012).
14. A. Kawase, S. Shirai, Y. Yamoto, R. Arakawa, and T. Takata, *Phys. Chem. Chem. Phys.*, **16**, 9344 (2014).
15. D. Zheng, X. Zhang, J. Wang, D. Qu, X. Yang, and D. Qu, *J. Power Sources*, **301**, 312 (2016).
16. J. Xiao et al., *Nano Lett.*, **15**, 3309 (2015).
17. N. A. Cañas, K. Hirose, B. Pascucci, N. Wagner, K. A. Friedrich, and R. Hiesgen, *Electrochim. Acta*, **97**, 42 (2013).
18. Z. Deng, Z. Zhang, Y. Lai, J. Liu, J. Li, and Y. Liu, *J. Electrochem. Soc.*, **160**, A553 (2013).
19. U. Gulzar, T. Li, X. Bai, M. Colombo, A. Ansaldo, S. Marras, M. Prato, S. Goriparti, C. Capiglia, and R. Proietti Zaccaria, *ACS Appl. Mater. Interfaces*, **10**, 5551 (2018).
20. Y.-C. Lu, Q. He, and H. A. Gasteiger, *J. Phys. Chem. C*, **118**, 5733 (2014).
21. P. Schön, F. Hintz, and U. Krewer, *Electrochim. Acta*, **295**, 926 (2019).
22. B. Zhang, J. Wu, J. Gu, S. Li, T. Yan, and X.-P. Gao, *ACS Energy Lett.*, **6**, 537 (2021).
23. J. Nelson, S. Misra, Y. Yang, A. Jackson, Y. Liu, H. Wang, H. Dai, J. C. Andrews, Y. Cui, and M. F. Toney, *J. Am. Chem. Soc.*, **134**, 6337 (2012).
24. D. R. Wang et al., *J. Electrochem. Soc.*, **165**, A3487 (2018).
25. H. L. Wu, L. A. Huff, J. L. Esbenshade, and A. A. Gewirth, *ACS Appl. Mater. Interfaces*, **7**, 20820 (2015).
26. Y. Gorlin, A. Siebel, M. Piana, T. Huthwelker, H. Jha, G. Monsch, F. Kraus, H. A. Gasteiger, and M. Tromp, *J. Electrochem. Soc.*, **162**, A1146 (2015).
27. Y. Gorlin, M. U. M. Patel, A. Freiberg, Q. He, M. Piana, M. Tromp, and H. A. Gasteiger, *J. Electrochem. Soc.*, **163**, A930 (2016).
28. D.-H. Han, B.-S. Kim, S.-J. Choi, Y. Jung, J. Kwak, and S.-M. Park, *J. Electrochem. Society*, **151**, E283 (2004).
29. E. Levillain, F. Gaillard, P. Leghie, A. Demortier, and J. P. Lelieur, *J. Electroanal. Chem.*, **420**, 167 (1997).
30. E. Levillain and F. Gaillard, *J. Electroanal. Chem.*, **398**, 77 (1995).
31. R. Bonnaterre and G. Cauquis, *J. Chem. Soc., Chem. Commun.*, 293 (1972).
32. Q. Zou and Y. C. Lu, *J. Phys. Chem. Lett.*, **7**, 1518 (2016).
33. X. Ma, H. Yang, Y. Li, X. Zhou, Z. Zhang, D. Duan, X. Hao, and S. Liu, *Chem. Eng. J.*, **427**, 131586 (2022).
34. C. Heubner, C. Lämmel, A. Nickol, T. Liebmann, M. Schneider, and A. Michaelis, *J. Power Sources*, **397**, 11 (2018).
35. C. Heubner, J. Seeba, T. Liebmann, A. Nickol, S. Börner, M. Fritsch, K. Nikolowski, M. Wolter, M. Schneider, and A. Michaelis, *J. Power Sources*, **380**, 83 (2018).
36. P. Bai and M. Z. Bazant, *Nat. Commun.*, **5**, 3585 (2014).
37. G. Férey, F. Millange, M. Morcrette, C. Serre, M.-L. Doublet, J.-M. Grenèche, and J.-M. Tarascon, *Angew. Chem. Int. Ed.*, **46**, 3259 (2007).
38. J. Li, X. Xiao, F. Yang, M. W. Verbrugge, and Y.-T. Cheng, *J. Phys. Chem. C*, **116**, 1472 (2011).
39. A. V. Ivanishchev, A. V. Churikov, I. A. Ivanishcheva, and A. V. Ushakov, *Ionics*, **22**, 483 (2015).
40. H. Lindstro, S. Sodergren, A. Solbrand, H. Rensmo, J. Hjelm, A. Hagfeldt, and S.-E. Lindquist, *J. Phys. Chem. B*, **101**, 7710 (1997).
41. R. Tian, P. J. King, J. Coelho, S.-H. Park, D. V. Horvath, V. Nicolosi, C. O'Dwyer, and J. N. Coleman, *J. Power Sources*, **468** (2020).
42. M. Metzger, P. Walke, S. Solchenbach, G. Salitra, D. Aurbach, and H. A. Gasteiger, *J. Electrochem. Soc.*, **167** (2020).
43. E. Umeshbabu, B. Zheng, J. Zhu, H. Wang, Y. Li, and Y. Yang, *ACS Appl. Mater. Interfaces*, **11**, 18436 (2019).

44. A. K. Yadav and P. Singh, *RSC Adv.*, **5**, 67583 (2015).
45. C. Han, M. Chen, R. Rasch, Y. Yu, B. Zhao, R. G. Reddy, P. Chaubal, P. C. Pistorius, and U. Pal, *Advances in Molten Slags, Fluxes, and Salts: Proceedings of the 10th International Conference on Molten Slags, Fluxes and Salts 2016, Editors, p. 175, Cham* (2016).
46. C. Luo, E. Hu, K. J. Gaskell, X. Fan, T. Gao, C. Cui, S. Ghose, X. Q. Yang, and C. Wang, *Proc Natl Acad Sci U S A*, **117**, 14712 (2020).
47. B. J. Lindberg, K. Hamrin, G. Johansson, U. Gelius, A. Fahlman, C. Nordling, and K. Siegbahn, *Phys. Scr.*, **1**, 286 (1970).
48. M. Kruk and M. Jaroniec, *Chem. Mater.*, **13**, 3169 (2001).
49. R. Tian, S. H. Park, P. J. King, G. Cunningham, J. Coelho, V. Nicolosi, and J. N. Coleman, *Nat. Commun.*, **10**, 1933 (2019).
50. R. Tian, N. Alcala, S. J. O'Neill, D. Horvath, J. Coelho, A. Griffin, Y. Zhang, V. Nicolosi, C. O'Dwyer, and J. N. Coleman, *ACS Appl. Energy Mater.*, **3**, 2966 (2020).
51. R. Tian, P. J. King, J. Coelho, S.-H. Park, D. V. Horvath, V. Nicolosi, C. O'Dwyer, and J. N. Coleman, *J. Power Sources*, **468**, 228220 (2020).
52. N. Kang, Y. Lin, L. Yang, D. Lu, J. Xiao, Y. Qi, and M. Cai, *Nat. Commun.*, **10**, 4597 (2019).